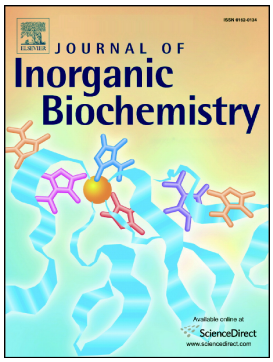

Pro-apoptotic activity of ruthenium 1-methylimidazole complex on non-small cell lung cancer

Júlia Scaff Moreira Dias, Henrique Vieira Reis Silva, Guilherme Álvaro Ferreira da Silva, Marisa Ionta, Charlane Cimini Corrêa, Fernando Almeida, Legna Colina-Vegas, Marília Imaculada Frazão Barbosa, Antônio Carlos Doriguetto

PII: S0162-0134(18)30189-2
DOI: doi:10.1016/j.jinorgbio.2018.06.008
Reference: JIB 10519

To appear in: *Journal of Inorganic Biochemistry*

Received date: 31 March 2018
Revised date: 12 June 2018
Accepted date: 13 June 2018

Please cite this article as: Júlia Scaff Moreira Dias, Henrique Vieira Reis Silva, Guilherme Álvaro Ferreira da Silva, Marisa Ionta, Charlane Cimini Corrêa, Fernando Almeida, Legna Colina-Vegas, Marília Imaculada Frazão Barbosa, Antônio Carlos Doriguetto , Pro-apoptotic activity of ruthenium 1-methylimidazole complex on non-small cell lung cancer. Jib (2018), doi:10.1016/j.jinorgbio.2018.06.008

Pro-apoptotic activity of ruthenium 1-methylimidazole complex on non-small cell lung cancer

Júlia Scaff Moreira Dias[a], Henrique Vieira Reis Silva[a], Guilherme Álvaro Ferreira da Silva[b], Marisa Ionta[b], Charlane Cimini Corrêa[c], Fernando Almeida[d], Legna Colina-Vegas[e], Marília Imaculada Frazão Barbosa[a*] and Antônio Carlos Doriguetto[a*]

[a] *Instituto de Química, Universidade Federal de Alfenas, CEP 37130-000, Alfenas-MG, Brazil.*

[b]*Departamento de Ciências Biomédicas, Universidade Federal de Alfenas, CEP 37130-000, Alfenas-MG, Brazil.*

[c]*Departamento de Química - ICE Universidade Federal de Juiz de Fora Campus CEP 36036-900, Juiz de Fora – MG, Brazil.*

[d]*Instituto de Ciências Biomédicas – icb4, Universidade de São Paulo, CEP 05508-900, São Paulo-SP, Brazil.*

[e]*Departamento de Química, Universidade Federal de São Carlos, CEP 13565-905, São Carlos-SP, Brazil*

[*] To whom correspondence should be addressed. *e-mail*: doriguetto@unifal-mg.edu.br (Antonio Carlos Doriguetto) and mariliaifrazaob@gmail.com (Marília I. F. Barbosa). Tel.: +55 35 3701-9712

Abstract

Herein, novel ruthenium(II) complexes containing 1-methylimidazole as a ligand were obtained with the following formulas: [RuCl(1Meim)(dppb)(bpy)]Cl (**1**), [RuCl(1Meim)(dppb)(4,4'-DMbpy)]Cl (**2**), [RuCl(1Meim)(dppb)(5,5'-DMbpy)]Cl (**3**) and [RuCl(1Meim)(dppb)(phen)]Cl (**4**) where, 1Meim = 1-methylimidazole, dppb = 1,4-Bis(diphenylphosphino)butane, bpy = 2,2'-bipyridine, 4,4'-DMbpy = 4,4'-dimethyl-2,2'-bipyridine, 5,5'-DMbpy = 5,5'-dimethyl-2,2′-bipyridine and phen = 1,10-phenanthroline. Additionally, crystal structures containing the cations of (**1**) and (**3**) were obtained when the counter ion was exchanged, leading to the formation of [RuCl(1Meim)(dppb)(bpy)]PF_6 (**5**) and [RuCl(1Meim)(dppb)(5,5'-DMbpy)]PF_6 methanol solvate (**6**) where PF_6 = hexafluorophosphate, showing one 1-methylimidazole molecule coordinated through the imidazole nitrogen, as expected. The complexes were characterized by elemental analysis, molar conductivity, infrared and UV-Vis spectroscopy, ^{1}H, $^{13}C\{^{1}H\}$ and $^{31}P\{^{1}H\}$ NMR, mass spectrometry and cyclic voltammetry. The interactions of complexes **1-4** with DNA and human serum albumin (HSA) were evaluated, and the cytotoxicity profiles of compounds **1-4** were determined using four different tumor cell lines derived from human cancers (melanoma: HT-144, colon: HCT-9, breast: MDA-MB-231 and lung: A549). A higher cytotoxic activity was observed for compound (**3**) against non-small cell lung cancer (A549). Complex (**3**) inhibited the clonogenic capacity and cell cycle progression of A549 cells and induced apoptosis involving mitochondrial pathway activation. Therefore, the data obtained in the present study support further investigations concerning molecular targets of complex (**3**) in non-small cell lung cancer.

Keywords: 1-methylimidazole; lung cancer; antitumor activity; ruthenium(II) complexes.

1. Introduction

The strong therapeutic properties of imidazole-related drugs have encouraged medicinal chemists to synthesize novel chemotherapeutic agents with this molecule to test against different diseases, including cancers [1-4]. It is relevant to improve therapeutic treatments for cancer patients, considering that cancer is a complex disease and was responsible for 8.8 million deaths in 2015, representing the second leading cause of death globally [5].

Ruthenium compounds such as [im][trans-$RuCl_4$(DMSO)(Him)], NAMI-A, [im][trans-$RuCl_4$(Him)] (im = imidazolium cation, Him = imidazole) and [ind][trans-$RuCl_4(Hind)_2$], KP1019, (ind = indazolium cation, Hind = indazole) are already progressing through clinical trials [2-4]. However, the antitumor mechanism of these ruthenium compounds is not fully understood [6–9]. NAMI-A has been characterized as antimetastatic agent, in particular for lung cancer, due to its ability of inhibiting *in vitro* cell migration and invasion [10-11]. The antimetastatic properties of KP1019 have also already been described [12]; however, it acts preferentially as a cytotoxic drug on primary tumors, especially on colorectal cancer, due to its pro-apoptotic and pro-oxidant activities [12].

Based on the interesting antitumor properties of imidazole derivatives and related properties of ruthenium, the present report describes the synthesis and characterization of Ru(II) complexes containing 1-methylimidazole (1Meim). The obtained complexes were evaluated for the ability to interact with DNA and human serum albumin (HSA). In addition, their *in vitro* antitumor potential was evaluated. By means of the A549 cell line, we demonstrated that the complex [RuCl(1Meim)(dppb)(5,5'-DMbpy)]Cl (dppb = 1,4-Bis(diphenylphosphino)butane and 5,5'-DMbpy = 5,5'-dimethyl-2,2′-bipyridine) is a promising antitumor agent against

lung cancer due to its ability to inhibit clonogenic capacity and cell cycle progression. We also demonstrated that the potent cytotoxic activity of this complex was due at least in part to its capacity to promote apoptosis.

2. Experimental Section

2.1. Materials for synthesis

Solvents were purified by standard methods. All chemicals used were of reagent grade or comparable purity. $RuCl_3 \cdot xH_2O$ and ligands 1-methylimidazole, 1,4-Bis(diphenylphosphino)butane, 2,2'-bipyridine (bpy), 4,4'-dimethyl-2,2'-bipyridine (4,4'-DMbpy), 5,5'-dimethyl-2,2'-bipyridine and 1,10-phenanthroline (phen) were used as received from Sigma-Aldrich.

2.2. Instrumentation

Elemental analyses were performed in a TruSpec CHNS-O model (Leco Instruments LTDA). The IR spectra were recorded on KBr pellets in the 4000-200 cm^{-1} region in a Bomen–Michelson FT MB-102 instrument. The UV-vis spectra were recorded in CH_2Cl_2 solution, in a Hewlett Packard diode array – 8452A. Cyclic voltammetry (CV) experiments were carried out at room temperature in CH_2Cl_2 solution containing 0.10 M $Bu_4N^+ClO_4$ (TBAP-Fluka Purum) using a BAS-100B/W Bioanalytical Systems instrument; the working and auxiliary electrodes were stationary Pt foils, a Luggin capillary probe was used, and the reference electrode was Ag/AgCl. All NMR experiments were recorded on a BRUKER, 300 MHz equipment, in a BBO 5 mm probe, at 298 K, and TMS for internal reference. For ^{1}H, $^{13}C\{^{1}H\}$, and $^{31}P\{^{1}H\}$ NMR spectra the $CDCl_3$-d was used as solvent. The splitting of proton, carbon and phosphorus resonances was reported as s = singlet, d = doublet, t = triplet, and m =

multiplet. The triple quadrupole mass spectrometer TSQ Quantum Max (Thermo Scientific) was operated at positive polarity and the ionization conditions were 240 °C for capillary temperature, 35 °C for vaporizer temperature, 3500 V for spray voltage and 5 bar for sheath gas pressure. The samples were analyzed by direct infusion using a 0.5 mL syringe and the samples were prepared in methanol at 10 $\mu g.mL^{-1}$ concentration.

2.3. X-ray crystallography

Well-shaped single crystals of (**5**) and (**6**) were chosen for the X-ray diffraction experiments that were performed at 298(2) K on an automatic diffractometer Agilent Technologies brand, Model SuperNova with graphite monochromated Mo-Kα radiation (λ = 0.71073 Å). The programs CrysAlis CCD and CrysAlis RED [13] were used for data collection, cell refinement, data reduction, and multi-scan method absorption correction. The structures were solved and refined using the software Sir2014 [14] and SHELXL-2013 [15], respectively. All atoms, except hydrogen, were clearly identified and refined by least squares full matrix F^2 with anisotropic thermal parameters. The hydrogen atoms bonded to carbons were stereochemically positioned following a riding model with fixed C—H bond lengths of 0.93, 0.96, and 0.97 Å for the aromatic, methyl and methylene groups, respectively. The hydrogen atom bonded to oxygen atom of the methanol molecule solvating the crystal structure of (**6**) were also stereochemically positioned following a riding model with idealized OH group (C-O-H angle tetrahedral and O—H bond length of 0.82 Å). The isotropic thermal parameters (Uiso) of all hydrogens depended on the equivalent isotropic thermal displacements of the atoms bonded to them [Uiso(H) = 1.2Ueq (C-aromatic and C-methylene) or 1.5Ueq (C-methyl and O-methanol). The crystallographic tables were generated by WinGX [16] and the structure representations by Mercury software [17] and $OLEX^2$ [18]. The main crystal

data collections and structure refinement parameters for (**5**) and (**6**) are summarized in Table 1. CCDC 1831213 and 1831214 contains the supplementary crystallographic data for (**5**) and (**6**). These data can be obtained free of charge from the Cambridge Crystallographic Data Centre (www.ccdc.cam.ac.uk/getstructures).

2.4. Synthesis

The precursors *cis*-[$RuCl_2$(dppb)(X-bpy)] or *cis*-[$RuCl_2$(dppb)(phen)], where X-bpy = 2,2'-bipyridine (bpy), 4,4'-dimethyl-2,2'-bipyridine (4,4'-DMbpy), 5,5'-dimethyl-2,2'-bipyridine (5,5'-DMbpy) and 1,10-phenanthroline (phen) were prepared according to literature [19]. Posteriorly, the ruthenium(II) 1-methylimidazole complexes with N-N = bpy (**1**), 4,4'-DMbpy (**2**), 5,5'-DMbpy (**3**) and phen (**4**) were prepared by reacting (0.06 mmol; ≅ 50 mg) of *cis*-[$RuCl_2$(dppb)(X-bpy)] with an excess of 1-methylimidazole ligand (0.30 mmol; = 0.024 mL) in 20 mL of dichloromethane previously degassed. The solution was kept under inert atmosphere and was stirred for 24 h. The final solution was concentrated to *ca.* 2 mL, and 10 mL of hexane was added to precipitate an orange powder. The solids were filtered off, washed with hexane and then dried under *vacuum*.

2.4.1 **[RuCl(1Meim)(dppb)(bpy)]Cl** (**1**) Yield: 38 mg (68%). Anal. Calc. for $C_{42}H_{42}Cl_2N_4P_2Ru$: exp.(calc) C, 60.50 (60.29); H, 5.08 (5.06); N, 6.73 (6.70). m/z exp.(calc): $C_{42}H_{42}ClN_4P_2Ru$ - 801.10 (801.27) $[M]^+$. $^{31}P\{^1H\}$ NMR (121.50 MHz, $CDCl_3$-d, 298 K): δ(ppm) 38.8 and 39.6 (d) Hz ($^2J_{P\text{-}P}$= 35.4 Hz). ^1H NMR (300 MHz, $CDCl_3$-d, 298 K): δ(ppm) 8.97 (s, CH-1Meim-H2), 8.37 (s, CH-1Meim-H1), 6.84 (s, CH-1Meim-H3), 7.75-6.50 overlapped signals, 29 H aromatic hydrogen for dppb, 3.15 (s, CH_3-1Meim-H4), and (8H, CH_2 of dppb) 4.00-1.0. $^{13}C\{^1H\}$ NMR (75.46 MHz,

$CDCl_3$-d, 298 K): δ(ppm) 138.25 (C-1 of 1Meim), 138-120 overlapped signals and 34.37 (C-4 of 1Meim). UV-Vis (CH_2Cl_2, 5.18 x 10^{-5} M): λ/nm (ε/M^{-1} L cm^{-1}) 288 (21.035), 332 (shoulder), 448 (3.668).

2.4.2 **[RuCl(1Meim)(dppb)(4,4'-DMbpy)]Cl** (**2**) Yield: 36 mg (65%). Anal. Calc. for $C_{44}H_{46}Cl_2N_4P_2Ru$: exp. (calc) C, 61.33 (61.11); H, 5.34 (5.36); N, 6.46 (6.48). m/z exp.(calc): $C_{44}H_{46}ClN_4P_2Ru$ 829.18 (829.33) $[M]^+$. $^{31}P\{^1H\}$ NMR (121.50 MHz, $CDCl_3$-d, 298 K): δ(ppm) 38.6 and 40.1 (d) MHz ($^2J_{P-P}$= 34.6 Hz). ^1H NMR (300 MHz, $CDCl_3$-d, 298 K): δ(ppm) 8.86 (s, CH-1Meim-H2), 8.56 (s, CH-1Meim-H1), 6.85 (s, CH-1Meim-H3), 7.75-6.50 overlapped signals, 29 H aromatic hydrogen for dppb, 3.15 (s, CH_3-1Meim-H4) and (8H, CH_2 of dppb) 4.00-1.0. $^{13}C\{^1H\}$ NMR (75.46 MHz, $CDCl_3$-d, 298 K): δ(ppm) 138.32 (C-1 of 1Meim), 138-120 overlapped signals and 34.18 (C-4 of 1Meim). UV-Vis (CH_2Cl_2, 5.33 x 10^{-5} M): λ/nm (ε/M^{-1} L cm^{-1}) 286 (19.137), 330 (shoulder), 440 (3.189). m/z 829.18 $[M]^+$

2.4.3 **[RuCl(1Meim)(dppb)(5,5'-DMbpy)]Cl** (**3**) Yield: 36 mg (65%). Anal. Calc. for $C_{44}H_{46}Cl_2N_4P_2Ru$: exp. (calc) C, 61.28 (61.11); H, 5.38 (5.36); N, 6.50 (6.48). m/z exp.(calc): $C_{44}H_{46}ClN_4P_2Ru$ - 829.14 (829.33) $[M]^+$. $^{31}P\{^1H\}$ NMR (121.50 MHz, $CDCl_3$-d, 298 K): δ(ppm) 38.6 and 40.1 (d) MHz ($^2J_{P-P}$= 35.4 Hz). ^1H NMR (300 MHz, $CDCl_3$-d, 298 K): δ(ppm) 8.97 (s, CH-1Meim-H2), 8.37 (s, CH-1Meim-H1), 6.82 (s, CH-1Meim-H3), 3.18 (s, CH_3-1Meim-H4), 7.75-6.50 overlapped signals, 29 H aromatic hydrogen for dppb and (8H, CH_2 of dppb) 4.00-1.0. $^{13}C\{^1H\}$ NMR (75.46 MHz, $CDCl_3$-d, 298 K): δ(ppm) 138.50 (C-1 of 1Meim), 138-120 overlapped signals and 34.44 (C-4 of 1Meim). UV-Vis (CH_2Cl_2, 4.92 x 10^{-5} M): λ/nm (ε/M^{-1} L cm^{-1}) 294 (20.935), 304 (shoulder), 432 (3.862). m/z 829.14 $[M]^+$

2.4.4 **[RuCl(1Meim)(dppb)(phen)]Cl** (**4**) Yield: 33 mg (60%). Anal. Calc. for $C_{44}H_{42}Cl_2N_4P_2Ru$: exp.(calc) C, 61.59 (61.40); H, 4.94 (4.92); N, 6.49 (6.51). m/z exp.(calc): $C_{44}H_{42}ClN_4P_2Ru$ - 825.14 (825.30) $[M]^+$. $^{31}P\{^1H\}$ NMR (121.50 MHz, $CDCl_3$-d, 298 K): δ(ppm) 38.5 and 39.1 (d) MHz ($^2J_{P\text{-}P}$= 34.6 Hz). ^1H NMR (300 MHz, $CDCl_3$-d, 298 K): δ(ppm) 9.41 (s, CH-1Meim-H2), 9.03 (s, CH-1Meim-H1), 6.88 (s, CH-1Meim-H3), 3.09 (s, CH_3-1Meim-H4), 7.75-6.50 overlapped signals, 29 H aromatic hydrogen for dppb and (8H, CH_2 of dppb) 4.00-1.0. $^{13}C\{^1H\}$ NMR (75.46 MHz, $CDCl_3$-d, 298 K): δ(ppm) 138.18 (C-1 of 1Meim), 138-120 overlapped signals and 34.18 (C-4 of 1Meim). UV-Vis (CH_2Cl_2, 4.60 x 10^{-5} M): λ/nm (ε/M^{-1} L cm^{-1}) 268 (23.913), 426 (652).

2.4.5 **[RuCl(1Meim)(dppb)(bpy)]PF_6** (**5**) and **[RuCl(1Meim)(dppb)(5,5'-DMbpy)]PF_6** (**6**)

The synthesis of complexes (**5**) and (**6**) was performed similarly to the others however, NH_4PF_6 was added to counter ion exchange. In a schlenk flask 50 mg (0.06 mmol) of the precursor *cis*-[$RuCl_2$(dppb)(X-bpy)], (X-bpy) = bpy (**5**) and 5,5'-DMbpy (**6**), with an excess of 1-methylimidazole ligand (0.30 mmol; = 0.024 mL) were added in 20 mL of dichloromethane previously degassed, then 20.8 mg (0.128 mmol) of NH_4PF_6 were added and the solution was kept under inert atmosphere and stirred for 4 h. The final solution was concentrated to *ca.* 2 mL, and 10 mL of hexane was added to precipitate an orange powder. The solids were filtered off, washed with hexane and then dried under *vacuum*. Single-crystals of the complexes (**5**) and (**6**), which were used only in the X-ray diffraction experiment, were grown from the evaporation of their solutions in CH_2Cl_2/CH_3OH (6:4 *v/v*).

2.5. Biological assays

2.5.1 Cell lines and treatment schedule

The following cell lines derived from human cancers were used in the present study: A549 (lung), HCT-9 (colon), HT-144 (melanoma), and MDA-MB-231 (breast). Fibroblasts (CCD-1059Sk) derived from normal skin were also examined. The cell cultures were maintained in DMEM (Dulbecco's Modified Eagle's Medium, Sigma, CA, USA) supplemented with 10% fetal bovine serum (Vitrocell, Campinas, Brazil). Cells were grown in a 37 °C humidified incubator containing 5% CO_2. The Ru(II) complexes were solubilized in DMSO immediately before use, and the amount of DMSO in the culture medium did not exceed 0.4% (v/v). Cells were seeded into 96-well plates (cell viability assay), 12-well plates (annexin V assay), or 35 mm Petri plates (cell cycle analysis). After attachment (24 h), the cultures were treated with different complexes over 24 h.

2.5.2 Cell viability analysis

Cell viability was measured by MTS (dimethylthiazol carboxymethoxyphenyl sulfophenyl tetrazolium) assay using the CellTiter 96® Aqueous Non-Radiative Cell Proliferation assay (Promega) according to the manufacturer's instructions. The MTS tetrazolium compound is bioreduced by metabolically active cells to give a colored formazan product that absorbs light at 490 nm. Viable cells rate is directly proportional to the amount of formazan produced by dehydrogenase enzymes. The experiments were conducted in triplicate wells and repeated twice. The data are presented as the mean ± standard deviation (SD). The cells were seeded into 96-well plates at a density of 5 x 10^3 cells/well (A549) or 1 x 10^4 cells/well (HCT-9, MDA-MB-231, and HT-144). The complexes (**1** – **4**) were used at 20 μM (A549 cell line) or 40 μM (A549, HCT-9, MDA-

MB-231, and HT-144) over 24 h for evidencing the most promising complexes. In next step, complexes (**3**) was evaluated in different concentrations (0 - 80 µM) for 24 h. IC_{50} values were determined from non-linear regression using GraphPad Prism® (GraphPad Software, Inc., San Diego, CA, USA).

2.5.3 Cell cycle analysis

Cell cycle analysis was performed according to literature [20]. Briefly, cells were treated with complex (**3**) for 24h at 5, 10 or 20 µM. Cells were fixed with 75% ethanol at 4 °C overnight and rinsed twice with cold phosphate-buffered saline (PBS). Afterwards, the cells were homogenized in a dye solution [PBS containing 30 $\mu g.mL^{-1}$ propidium iodide (PI) and 3 $mg.mL^{-1}$ RNAase]. DNA was quantified 1h after staining. The analysis was performed by flow cytometry (Guava easyCyte 8HT, Hayward, CA, USA). Results are presented as the mean ± SD of three independent experiments.

2.5.4 Clonogenic assay

The clonogenic assay was performed according to [21] with some modifications. Briefly, 100 cells were seeded into 35mm Petri plates. The cells were treated for 24h with complex (**3**) at a concentration of 5, 10, or 20 µM and recovered in a drug-free medium for an additional 15 days. Afterwards, the colonies were fixed and stained with crystal violet. Only the colonies with > 50 cells were counted by direct visual inspection with a stereomicroscope at 20 × magnification. Assays were performed in triplicate, and the data are presented as the mean ± SD of three independent experiments.

2.5.5 Apoptosis evaluation using annexin V assay

Cells were seed into 12-well plates at 8×10^4 cells/well. After 24 h of treatment with complex (**3**) at a concentration of 10 or 20 µM, we evaluated the

phosphatidylserine externalization using Guava Nexin® Kit (Merck Millipore, Massachusetts, USA) according to manufacturer's instructions. Briefly, cells were collected by enzymatic digestion (Trypsin/EDTA, Sigma), centrifuged at 1,000 rpm for 5 min at 4 °C, and washed with ice-cold PBS, and then 2×10^4 cells were resuspended in 100 µL of DMEM. In the next step, 100 µL of a mixed solution containing buffered Annexin V-PE and 7-AAD was added. The samples were read after 20 min of incubation at room temperature in a dark chamber. The analysis was performed by flow cytometry using GuavaSoft 2.7 software. The experiments were conducted in triplicate and repeated twice. The data are presented as the mean ± SD.

2.5.6 Mitochondrial membrane potential (ΔΨm) analysis by JC-1 fluorescence

The alteration of ΔΨm in A549 cells were analyzed through a JC-1 staining using Guava®MitoPotential Kit (Merck/millipore) according to manufacturer's instructions. Briefly, the cells were trypsinized and washed twice with PBS; after that, the cells were labeled with the fluorescent dye JC-1/7-AAD in the dark chamber for 30 min at 37 °C. Carbonyl cyanide m-chlorophenyl hydrazone (CCCP) was used as a positive control to reduce ΔΨm. The analysis was performed by flow cytometry using GuavaSoft 2.7 software. The data are shown as mean ± SD from three independent experiments.

2.5.7 ATM activation profile

Ataxia telangiectasia-mutated (ATM) activation was measured by flow cytometry (software GuavaSoft 2.7) using Cell Cycle Checkpoint ATM DNA Damage Kit (Merck-millipore) according to manufacturer's instructions. Briefly, the cells were trypsinized, washed twice and fixed. After permeabilization process, anti-p-ATM

(Ser1981) was incubated por 1 h (4 °C in dark chamber). The nuclei were stained with Propidium iodide for 30 min. The data are shown as mean ± SD from three independent experiments.

2.5.8 Statistical Analysis

The results of the biological assays were tested for significance using one-way analysis of variance (ANOVA) followed by Tukey's post-test using GraphPad Prism®. The values are expressed as the mean ± SD.

2.5.9 HSA fluorescence

Fluorescence spectroscopy is an effective method for exploring the interactions between small molecules and biomacromolecules. The fluorescence of HSA comes from its tryptophan, tyrosine and phenylalanine residues, where the latter two contribute to its fluorescence to only a minor extent [22]. The protein interaction was examined in 96-well plates used for fluorescence assays. HSA (~2.5 x 10^{-6} mol·L^{-1}) was prepared by dissolving the protein in Tris–HCl at pH = 7.4, and the complexes were dissolved in sterile DMSO. For the fluorescence measurements, the HSA concentration in the buffer Tris–HCl was kept constant in all samples, while the complex concentration was increased from 0.78 to 100 μM, and quenching of the emission intensity of the HSA tryptophan residues at 305 nm (excitation wavelength of 270 nm) was monitored at different temperatures (298 and 310 K). A standard solution was prepared with 180 μL of albumin and 20 μL of DMSO. The experiments were carried out in triplicate and analyzed using the classical Stern–Volmer equation as follows:

$$F_0/F = 1 + K_q\tau_o[Q] = 1 + K_{sv}[Q] \quad \text{Eq. (1)}$$

where F_0 and F are the fluorescence intensities in the absence and presence of quencher, respectively, [Q] is the quencher concentration, and Ksv is the Stern–Volmer quenching constant, which can be written as $Kq= Ksv/\tau_o$, where Kq is the bimolecular quenching rate constant and τ_o is the average lifetime of the fluorophore in the absence of quencher (6.2×10^{-9} s) [23]. Therefore, Eq. (**1**) was applied to determine Ksv by linear regression of a plot of Fo/F vs. [Q].

The binding constant (Kb) and the number of complexes bound to HSA (n) were determined by plotting the double logarithmic graph of the fluorescence data using Eq. (**2**) as follows:

$$\log [(F_0-F)/F] = \log Kb + n\log [Q] \quad \text{Eq. (2)}$$

The thermodynamic parameters were calculated from the eq. (**3**):

$$\ln (K_2/K_1) = [(1/T_1)-(1/T_2)]\, \Delta H/R \quad \text{Eq. (3)},$$

where K_1 and K_2 are the binding constants at temperatures T_1 and T_2, respectively, and R is the gas constant. Furthermore, the change in free energy (ΔG) was calculated from Eq. (**4**):

$$\Delta G = -RT \ln K = \Delta H - T\Delta S \quad \text{Eq. (4)}$$

The inner filter effect on the intensity of fluorescence of the protein and complexes were corrected according to the Eq (**5**) where F_{corr} and F_{obs} are the corrected and observed fluorescence intensities and A_{ex} and A_{em} are the absorbance values at excitation and emission wavelengths.

$$F_{corr} = F_{Obs}\, e^{\frac{(A_{em}+A_{ex})}{2}} \quad \text{Eq. (5)}$$

2.5.10 DNA interaction studies

The interactions of the complexes with ctDNA (calf thymus DNA) were analyzed by absorption spectrophotometric analysis at room temperature using a Hewlett Packard diode array – 8452 UV–vis spectrophotometer. A standard solution of calf thymus DNA (ctDNA) from Sigma-Aldrich was prepared in Tris-HCl buffer (5 mM Tris–HCl and 50 mM NaCl, pH 7.4). The concentration of this ctDNA solution was determined from its absorption intensity at 260 nm using a molar absorption coefficient value of 6600 M^{-1} cm^{-1}. The ctDNA solution was protein-free given that the ratio of the UV absorbances at 260 and 280 nm was approximately 1.8-2.0. The absorption titrations were recorded in the range of 200–450 nm while keeping the concentration of the Ru(II) complexes constant (1.0 mM) and increasing the amount of ctDNA after each addition. The intrinsic equilibrium binding constant (Kb) of the complexes to ctDNA was obtained by monitoring the changes in the absorption intensity with increasing concentration of ctDNA and analyzed by regression analysis.

3. Results and discussion

3.1. Synthesis

The reaction of 1-methylimidazole with ruthenium precursors *cis*-[$RuCl_2$(dppb)(X-bpy)] or *cis*-[$RuCl_2$(dppb)(phen)] was employed to obtain the complexes [RuCl(1Meim)(dppb)(bpy)]Cl (**1**), [RuCl(1Meim)(dppb)(4,4'-DMbpy)]Cl (**2**), [RuCl(1Meim)(dppb)(5,5'-DMbpy)]Cl (**3**) and [RuCl(1Meim)(dppb)(phen)]Cl (**4**) by single chloride exchange under mild conditions (Scheme 1).

The elemental analyses are described in the experimental section, and they agreed well with the proposed formulations. The MS spectra were acquired in the positive mode, and the charged complex ions resulting from loss of the respective chloride ions were observed (Supporting material: **Figures 1S-4S**). The molar

conductance values measured for complexes (**1-4**) in acetone at room temperature ranged from 93.3 to 113.9 $S.cm^2.mol^{-1}$, revealing 1:1-type compounds [24]. Furthermore, the complexes were characterized by $^{31}P\{^1H\}$, $^{13}C\{^1H\}$ and ^1H NMR spectroscopy, UV-Vis and IR spectroscopy, and cyclic voltammetry. Compounds (**5**) and (**6**), which contained the cations present in (**1**) and (**3**), respectively, had their structures determined by X-ray crystallography, confirming the coordination sphere around the Ru(II) cation containing the imidazole molecule (details in section **3.2**).

The $^{31}P\{^1H\}$ NMR spectra of complexes (**1-4**) in $CDCl_3$ presented a typical AX spin system, indicating the magnetic nonequivalence of the two phosphorus atoms, in which one is *trans* to the N (X-bpy or phen) ligand and the other is *trans* to the N of the 1-methylimidazole ligand (Supporting material: **Figure 5S-8S**)**.** The chemical shifts and coupling constants ($^2J_{P\text{-}P}$) are shown in the experimental section. For all complexes, the $^{31}P\{^1H\}$ NMR chemical shifts were different from those of the *cis*-[$RuCl_2$(dppb)(X-bpy)] or *cis*-[$RuCl_2$(dppb)(phen)] starting material, suggesting that the presence of a 1-methylimidazole ligand coordinated to the metal shifted the electron density of the phosphorus atoms of the dppb ligand.

In the ^1H NMR spectrum of the free 1-methylimidazole, a singlet at 3.64 ppm assigned to the methyl group and signals at 7.39, 7.06 and 6.86 ppm assigned to H1, H2 and H3 were observed (Scheme 1). For all complexes, H1 and H2 characteristic deshielded signals at 9.41-8.37 and 9.03-8.37 ppm, respectively, were observed, as expected, due to imidazolic nitrogen coordination. Other aromatic hydrogen atom resonances were in the range 5.00–8.00 ppm and were attributed to the protons present in the aromatic phosphine and X-bpy or phen ligands. Additionally, 8 hydrogens of the CH_2 groups of dppb were observed at 4.00-1.0 ppm. All complex spectra exhibited a

singlet at 3.18-3.09 ppm assigned to the methyl group of 1-methylimidazole (Supporting material: **Figure 9S-12S**).

The chemical shifts of the $^{13}C\{^{1}H\}$ NMR spectra for the free 1-methylimidazole and their respective complexes are summarized in Table S1 (Supporting material). All of the complex signals ranging from 33.05-34.44 ppm were attributed to the methyl group C4, and signals at 138.18-138.66 ppm were relative to C1, whereas signals referent to C4 and C1 in the free ligand were observed at 33.14 ppm and 137.79. Aromatic carbon atoms of X-bpy, phen and phosphine were also identified in the range of 170–120 ppm (Supporting material: **Figure 13S-16S**).

Time-dependent $^{31}P\{^{1}H\}$ NMR experiments in solution were carried out to evaluate the stability of the complexes. Thus, the complexes were diluted in DMSO and analyzed from 0 to 48 h (Supporting material: **Figures 17S-20S**). The $^{31}P\{^{1}H\}$ NMR spectra reveal that all complexes (**1-4**) were stable over this length of time.

Infrared spectra of the complexes presented characteristic bands due to 1-methylimidazole, X-bpy or phen and dppb ligand vibrations (Supporting material: **Figures 21-25S**). The stretching modes of the aromatic imidazole C–H bonds displayed maxima ranging from 3126 to 3132 cm^{-1}. The strong band at 1521 cm^{-1} was assigned to ν(C=C). The methyl groups of the 1Meim ligand were indicated by bands near 2920, 2922, 2924 and 2920 cm^{-1}, respectively, for complexes (**1-4**). The ν(C=N) of the imidazole ring appeared close to 1629, 1622, 1624 and 1625 cm^{-1} for compounds (**1-4**), respectively, which was different from that of the free ligand (1649 cm^{-1}) and indicated the coordination of the ligand by the imidazolic nitrogen atom. The low-intensity band ranging from 485 to 489 cm^{-1} was assigned to the νRu-N stretch [25]. Table **2** summarizes the main IR frequencies (cm^{-1}) of 1-methylimidazole and complexes (**1-4**).

The electronic spectra of complexes (**1-4**) (Supporting material: **Figures 26S-29S**) showed two bands in the UV region (268–304 nm) assigned to $\pi \rightarrow \pi^*$ transitions, which were also present in the spectra of the free dppb and diimine ligands [26, 27]. The bands at approximately 440 nm were attributed to metal-to-ligand charge transfer, probably from ruthenium to the diimine, pyridine and dppb ligands. Similar assignments have been proposed for other Ru(II) complexes [28].

The electrochemical behavior of complexes (**1-4**) containing the 1-methylimidazole ligand was similar to that found for other Ru(II) complexes presenting diimine and dppb ligands [29] (Supporting material: **Figures 30S-33S**). These experiments were performed under the same conditions, and it was observed that complexes (**1-4**) exhibited a *quasi*-reversible process assigned to the redox pair Ru(II)/Ru(III), with E*pa* ranging from 1010 to 1080 mV. The spectral difference observed among the complexes may be due to their stereochemistry differences. The E½ values found for the complexes were considerably more anodic than those observed for both precursors $[RuCl_2(dppb)(X\text{-}bpy)]$ and $[RuCl_2(dppb)(phen)]$ [19], indicating that the ruthenium center was more stable after coordination with 1-methylimidazole than was the precursor. The metal center stabilization occurred due to replacement of a chloride by an imidazolic nitrogen of 1-methylimidazole. A linear correlation of the pKa values of the X-bpy ligands with the redox potential of the complexes were observed (Supporting material: **Table S1**). The lowest redox potential of complex (**3**) could be correlated with the highest activity against A549 cells. In general, the redox activity of Ru complexes is associated with the formation of ROS in cells and might lead to activation in the reductive environment of tumors (30).

3.2. Single-Crystal X-ray Analysis

Attempts to obtain a single crystal of (**1-4**) for X-ray diffraction experiments were all unsuccessful. Therefore, an attempt was also made to obtain single crystals containing the large cations of (**1-4**) by replacing chloride with hexafluorophosphate (PF_6). These experiments were successful for crystal growth of (**5**) and (**6**). When the small chloride counter-ion was exchanged, single crystals containing the large cations of (**1**) and (**3**) were obtained containing the large PF_6^- counter-ion, leading to formation of (**5**) and (**6**), respectively. This provides examples of the general principle that solid salts separate from aqueous solutions easiest in combinations of either small cation-small anion or large cation-large anion (as here), preferably with systems having the same but opposite charges on the counter-ions [31]. The entrance of solvent into the crystalline lattice also helped in the crystallization of (**6**).

The X-ray structures shown in **Figure 1** confirm that (**5**) and (**6**) were six-coordinate complexes of a ruthenium cation bound to the P1 and P2 phosphorous atoms from the dppb ligand, the N1 and N2 nitrogen atoms from the bipyridines bpy (**5**) and 5,5'-DMbpy in (**6**), the N3 nitrogen atom from the 1-methylimidazole ligand, and the chlorido anion. The 1Meim ligand was positioned *cis* to the coordinated chlorido ligand and *trans* to the P2 atom from the dppb ligand. Considering the precursors *cis*-[$RuCl_2$(dppb)(bpy)] [19] and *cis*-[$RuCl_2$(dppb)(5,5'-DMbpy)] [32], it was confirmed that the 1Meim ligand replaced the chlorido ligand *trans* to the dppb phosphorous atom, in agreement with analogous complexes [25, 33-38]. A molecular superposition of (**5**) and (**6**) (overlaid using the Ru atoms and the six atoms coordinated to them as homologous atom pairs) showed that the two complexes differed significantly in the orientation of the phenyl groups linked to the dppb ligand P2 atom (**Figure 1c**).

Analysis of the octahedral geometry around the Ru cation in (**5**) and (**6**) showed that for both structures, as expected, the smallest metal-ligand distances involved the

nitrogen atoms (N1 and N2) from the bipyridines (bpy or 5,5`-DMbpy ligands), whereas the largest distances were between the Ru metal and the chlorido ligand (**Table 3**). The bond lengths of the Ru-P2 were comparable to those of Ru-P1 in either (**5**) or (**6**). This structural feature was also expected in (**5**) and (**6**), taking into account that their respective P1 and P2 phosphorus atoms were both *trans* to the nitrogen atoms (N1 and N2) from the bipyridines. Therefore, the two phosphorous atoms were not susceptible to different *trans* competitions, as observed in the analogous complex having a P2 *trans* to the CO ligand [28, 37]. The Ru-N3 distances in (**5**) and (**6**) did not present a significant difference (**Table 3**) and were very similar to those observed for the analogous complexes having pyridines instead of 1Meim groups completing their coordination sphere, including pyridine (Ru-N3 = 2.215(3) Å) [25], 4-methylpyridine (Ru-N3 = 2.175(7) Å) [34], 4-amine-pyridine (Ru-N3 = 2.203(4) Å) [25], 4-phenylpyridine (Ru-N3 = 2.170(3) Å) [38] or 4-vinylpyridine (Ru-N3 = 2.213(3) Å) [39]. Finally, upon comparing the bond angle values around the octahedral Ru coordination sphere (**Table 3**), it was observed that the largest deviation from the orthonormality involved the two nitrogen atoms (N1-Ru-N2 angle) from the bipyridinic rigid bidentate ligand, which was also in agreement with other analogous complexes [25, 28, 33-39].

As emphasized in our previous work [37], the overall geometries of the compounds with the general formula ct-[RuCl(L)(dppb)(bipyridine)] having L *cis* to the chlorido ligand and *trans* to dppb were very similar. Therefore, confirming our expectation, the intramolecular geometry of (**5**) was similar to those observed for the analogous complexes containing one bpy and one dppb as bidentate ligands and one chlorido and one pyridine-derivative (pyridine [25], 4-methylpyridine [34], 4-amine-pyridine [25] or 4-phenylpyridine [38]) as monodentate ligands (Supporting material: **Figure 35S**).

A very interesting aspect of the crystallographic part of the present work is the finding that (**6**) and its analogous *cis*-[RuCl(4-vinylpyridine)(dppb)(5,5`-Mebipy)] [39] (5,5`-Mebipy = 5,5'-dimethyl-2,2′-bipyridine), were crystals with isotype features [40]. That means, in spite of the different chemical compositions (the crystal structure of (**6**) had the 1Meim ligand instead 4-vinylpyridine in addition to being solvated by methanol), they crystallized in the same space group (Pbca) with very similar unit cell metrics (a = 15.0023(3), b = 20.3898(3), and c = 29.2586(6) Å in (**6**) *vs.* a = 14.669(3), b = 20.499(3), and c = 29.401(6) Å in the 4-vinylpyridine analogue [39] and had comparable fractional atomic coordinates for the homologous atoms (Ru, Cl, dppb and 5,5'-DMbpy) (**Figure 2**) and equivalent intermolecular arrays (packing) (**Figure 3**).

Even though the term "very similar" has not been defined in quantitative terms, [41] the unit cell dimensions of these isotype crystals are expected to be slightly different as a consequence of their different chemical compositions. Moreover, since 1Meim is smaller than 4-vinylpyridine, it would be expected that the unit cell of (**6**) was smaller than that of the 4-vinylpyridine analogue. However, this was only observed with respect to their respective b and c-axes. The a-axis of (**6**) was 0.333 Å longer than that of its previously reported analogue. Closer scrutiny showed that the a-axis increase in (**6**) was a consequence of solvent insertion and not ligand replacement (**Figure 3**). In the specific case discussed here, these two variables are, of course, correlated, since to retain the same structure, the void left by replacing a larger ligand (4-vinylpyridine) with a smaller one (1Meim) had to be filled by the solvent (methanol) to stabilize the packing of (**6**). It is important to emphasize that the void volume occupied by the methanol molecule in (**6**) was 3% (272.50 $Å^3$) of its unit cell volume (calculated by MERCURY [17] using a grid spacing of 0.7 Å and probing-sphere radius of 1.1 Å). It is also important to note that the difference in volume between the two unit cells was only

1.2% (8950 $Å^3$ in (**6**) *vs.* 8841 $Å^3$ in its analogue). The contact surfaces of the calculated voids in (**6**) occupied by methanol are shown in (Supporting material: **Figure 36S**). It is relevant to mention that the differentiation of isotype crystals by PXRD analysis could be a difficult task since their PXRD patterns are expected to be almost identical, which was confirmed here by comparing the calculated PXRD patterns to the crystal structures of (**6**) and its analogue (CCDC code BUZYIF [39]) (Supporting material: **Figure 37S**).

3.3. Biological targets: DNA and HSA binding studies

3.3.1 **Fluorescence spectra of HSA–Ru complexes**

HSA solutions exhibit a strong fluorescence emission with a peak at 338 nm, which is provided mainly by a single residue of tryptophan located at position 214 along the chain in subdomain IIA [42, 43]. To understand the mechanism of interaction between complexes (**1-4**) and HSA, fluorescence quenching experiments were performed. The experiments were carried out by holding the concentration of the HSA solution constant and adding increasing concentrations of complexes (**1-4**) at temperatures of 298 and 310 K while monitoring the fluorescence intensity suppression. The effects of the complexes on the protein fluorescence intensity are presented in (Supporting material: **Figure 38S**). The constants obtained for complexes (**1-4**) are listed in **Table 4**.

The K_{SV} values displayed an inverse correlation with the temperature, which suggested that this quenching mechanism was static and initiated by adduct formation [44]. The binding constants acquired have been ranked as 4 > 3~2 > 1, indicating a more potent interaction between HSA and complex (**4**). This conduct may be related to the size and electronic density of the phenantroline ligand, which is a larger substituent and a better activator than bipyridine and methyl-bipyridine. The quantity of the binding

sites (n) was approximately 1, indicating at least one binding site with HSA. The thermodynamic parameters (ΔH^o, ΔS^o and ΔG^o) were obtained to evaluate the intermolecular forces between the complexes and the protein. As observed in **Table 4**, for compounds (**1**, **2** and **3**), the negative ΔH^o and ΔS^o values reflect van der Waals forces or hydrogen bond formation, whereas for complex (**4**), the positive ΔH^o and ΔS^o values indicate the predominance of hydrophobic interactions [22,45-47]. Furthermore, the negative ΔG^o values observed for all complexes reveal that the interaction was spontaneous. Thus, complexes (**1-4**) can be stored in the protein and released at targets.

The results are in agreement with those for other ruthenium compounds such as $[RuCl(CTZ)(bipy)(P\text{-}P)]PF_6$ (CTZ = clotrimazole, bipy = 2,2'-bipyridine and P-P = 1,2-bis(diphenylphosphino)ethane, 1,4-bis(diphenylphosphino)butane and 1,1'-bis(diphenylphosphino)ferrocene). CTZ, a kind of imidazole, binds to BSA with moderate affinity through a static quenching mechanism, and the thermodynamic parameters reveal the predominance of hydrophobic interactions with the protein [48].

3.3.2 DNA-binding: UV-Vis spectrophotometric titration

UV–visible absorption spectroscopy is a useful direct method for determining the DNA binding constants of metal complexes that can interact at distinct binding sites (groove binding outside of the DNA helix along the major or minor groove, electrostatic binding to a phosphate group and intercalation). To investigate DNA as a potential target for the complexes, spectroscopic studies were carried out. Upon adding the solution of ctDNA to each complex (**1–4**), a decrease in the absorption intensity (hypochromism) was observed, which suggests interaction between the complexes and ctDNA. A representative absorption spectrum of compound (**3**) is provided in **Figure 4,** and those for compounds (**1, 2** and **4**) are in (Supporting material: **Figure 39S**).

The magnitude of such interaction was indicated by the DNA binding constant, Kb, (**Table 5**) which was calculated according to Eq. 4 [34] as follows:

$$[ctDNA]/(\varepsilon_a-\varepsilon_f) = [ctDNA]/(\varepsilon_b-\varepsilon_f) + 1/Kb(\varepsilon_b-\varepsilon_f) \qquad \text{Eq. (4)}$$

where [ctDNA] is the concentration of ctDNA in base pairs, ε_a is the ratio of the absorbance/[Ru], ε_f is the extinction coefficient of the free Ru(II) complex, and ε_o is the extinction coefficient of the complex in the fully bound form. The ratio of the slope to the intercept in the plot of [DNA]/(εa-εf) *vs.* [DNA] gives the value of Kb, which was calculated from the metal-to-ligand charge transfer (MLCT) absorption band (λ_{max}) at 424 nm for complexes (**1-3**) and 400 nm for complex (**4**). The values obtained for the binding constant and the percentage of hypochromism for each complex are summarized in **Table 5.**

Compounds (**1-4)** interacted with DNA with binding constants, Kb, on the order of 10^4 M^{-1}. The magnitude of Kb found here is comparable with those of metal complexes that bind ctDNA through noncovalent (electrostatic or hydrogen bonding) interactions reported in the literature [33, 34], and such interactions that occur with other Ru(II)/phosphinic/diimine complexes, as reported elsewhere [33, 34, 48].

3.4. Biological assays

The complexes (**1-4**) were evaluated against 4 different tumor cell lines at 40 µM for 24 h. We observed significant cytotoxic activity by complex (**3**) on HT-144 and MDA-MB-231 when compared to control samples (**Figure 5A**). Interestingly, in these experimental conditions, all complexes displayed potent cytotoxicity against A549 cells, reducing almost 100% of cell viability (data not shown). Thus, the complexes were again evaluated on A549 cells at 20 µM, and results showed high cytotoxicity of

complex (**3**) (**Figure 5A**). Some studies have reported a great responsiveness of A549 cells to ruthenium complexes treatment when compared to other tumor cell lines [2, 20, 49-50]. This finding is very relevant, considering that A549 cells are derived from non-small cell lung cancer, a type of tumor that represents 75-80% of all lung cancers diagnosed [51].

We selected complex (**3**) to perform dose-response curves. We included in the analysis both the ruthenium complex precursor [$RuCl_2$(dppb)(5,5'-DMbpy)] and free 1-methylimidazole (ligand). We provided evidence that complex (**3**) was much more cytotoxic when compared to the precursor (**Figure 5B**). The IC_{50} value (**Table 6**) of the complex (**3**) was approximately 4-fold higher than that of cisplatin, and the ligand did not display cytotoxic activity on A549 cells, at least not in the concentration range tested. These findings evidence that the coordinated structure of the complex was critical for its cytotoxic activity, highlighting the importance of the positions of the metal [20] and methyl groups [52]. We also examined the cytotoxic profile of complex (**3**) on human normal fibroblasts, which was lower than that toward A549 cells (**Table 6**), indicating a certain selectivity of the tested compound toward tumor cells.

The morphological features of the A549 cells treated with complex (**3**) or the vehicle are shown in **Figure 6A**. A reduction in cell density was observed in all treated samples compared to untreated cultures. In addition, cell morphology was profoundly altered by treatment with complex (**3**) at 10 µM and 20 µM. Rounded cells were frequently observed in cultures treated with complex (**3**) at 20 µM, indicating cell detachment from the substrate, similarly to the process observed in cell death (**Figure 6A**).

In the next step, to better understand the biological mechanisms underlying complex (**3**) activity toward A549 cells, we verified whether complex (**3**) reduced

clonogenic capacity and/or promoted apoptosis in A549 cells. The data showed that the complex (**3**) was very cytotoxic at 10 and 20 µM once colonies were not observed in treated samples. Interestingly, we observed a significant reduction of the number of colonies in samples treated with complex (**3**) at 5 µM compared to the control group. In addition, there was a reduction in the diameter of the colonies, indicating that the proliferation rate of the A549 cells was affected by the treatment, even after drug removal (**Figure 6B** and **C**). These findings are very important, considering that the sustained proliferative behavior of tumor cells is critical for tumor progression and metastasis [53]. The negative influence of complex (**3**) on the proliferative behavior of A549 cells over a prolonged period demonstrates its promising antitumor potential. There are a few reports concerning the influence of ruthenium complexes on the clonogenic capacity of A549 cells. It has been reported that *cis*-$[RuCl_2(NH_3)_4]Cl$ [54] and $[Ru(pipe)(dppb)(bipy)]PF_6$ (pipe = piperonylic acid and bipy = 2,2'-bipyridine) [20] inhibited the colony-formation ability of A549 cells. However, these studies did not report reductions in colony diameters observed in the present study.

To investigate whether the antiproliferative activity of complex (**3**) on A549 cells was triggered by cell cycle arrest, we performed DNA quantification by flow cytometry using propidium iodide (PI) staining. We observed a significant increase of the G0/G1 population and reduction of the cell population at G2/M in cultures treated with complex (**3**) at sub-toxic concentrations (5 µM), indicating cell cycle arrest at the G1/S transition. We also observed an elevated subdiploid peak (sub-G1 phase) in samples treated with complex (**3**) at 10 and 20 µM compared to the control group, indicating complex (**3**) promoted an increase of the dead cell population. These findings corroborated the results obtained in the clonogenic assay and observations concerning cell morphology features. Accumulation of cells in the G0/G1 phase is often the result

of cell cycle checkpoint activation [55]. Studies have shown that some ruthenium compounds induce the arrest of cells in the G0/G1 phase by modulating the activity of important regulators of the G1/S transition including p53, p21, CDK4/6 and cyclin D1 [20, 56]. Further investigations will be performed to identify the molecular targets of complex (**3**) in A549 cells.

The pro-apoptotic activity of complex (**3**) was evaluated by a PE-Annexin assay based on its high cytotoxicity on A549 cells. We observed a frequency increase of annexin V-positive cells in cultures treated for 24 h at 10 and 20 µM (**Figure 6D**), indicating that apoptosis was effectively induced in treated samples in a concentration-dependent manner. Our data corroborate those reported by other authors demonstrating the pro-apoptotic activity of ruthenium complexes such as Ru(II)/phosphinic/diiminic complexes, *cis*-$[RuCl_2(NH_3)_4]Cl$ and $[Ru(pipe)(dppb)(bipy)]PF_6$ [20, 53]. Evasion of apoptosis is one of the central features of tumor progression and drug resistance [53]. Therefore, compounds that effectively induce apoptosis represent good candidates as antineoplastic agents.

We sought to investigate whether the pro-apoptotic activity of complex (**3**) toward A549 cells was related to activation of the intrinsic apoptotic pathway, also called the mitochondrial pathway. Thus, we verified the influence of this complex on the mitochondrial membrane potential ($\Delta\Psi m$) using the fluorescent probe JC-1, which exhibits $\Delta\Psi m$-dependent accumulation and emits strong orange fluorescence in normal mitochondria, while in unhealthy mitochondria, JC-1 emits a strong green fluorescence. We observed a strong reduction in the orange/green ratio in samples treated with complex (3) at 20 µM (**Figure 6E**), indicating a significant decrease of $\Delta\Psi m$ in A549 cells. Our data showed, therefore, that the pro-apoptotic activity of complex (**3**) is associated with intrinsic apoptotic pathway activation. Recent studies have

demonstrated that ruthenium complexes are effective in inducing apoptosis by mitochondrial pathway activation [20, 57]; however, the molecular target underlying this specific cellular response still remains unclear.

The intrinsic apoptotic pathway may be activated by various intracellular stress signals including DNA damage. Thus, we also evaluated the activation profile of ATM by flow cytometry in A549 cells treated with complex (**3**), considering that ATM (ataxia telangiectasia mutated) is a kinase protein critically involved in the DNA damage response induced by radiation or chemotherapeutic drugs. ATM is a member of the phospho inositide 3-kinase (PI3K)-related Ser/Thr protein kinase family. Inactive ATM exists as a dimer but quickly dissociates and becomes phosphorylated on serine 1981 in response to ionizing radiation. Activated ATM phosphorylates several key proteins that act as DNA damage checkpoints, leading to cell cycle arrest, DNA repair, or apoptosis [58]. We did not evidence a significant increase in ATM activation after treatment with complex (**3**) (**Figure 6F**), indicating that its pro-apoptotic activity on A549 cells was not directly associated with primary damage to DNA.

The findings obtained in the present study are very promising and support further molecular studies to identify the probable molecular targets for complex (**3**) in non-small cell lung cancer.

4. Conclusions

This report presents the synthesis and characterization of four new cationic ruthenium complexes with X-bpy or phen and 1-methylimidazole. Crystal structures containing the cations of (**1**) and (**3**) were obtained when the counter ion was exchanged. A linear correlation of the pKa values of the X-bpy ligands with the redox

potential of the complexes was observed. The lowest redox potential of complex (**3**) could be correlated with the higher active against A549 cells.

Interactions with DNA and human serum albumin (HSA) were performed with (**1-4**), and it was found that Ru(II)-complexes exhibit moderate DNA-binding affinity. The HSA binding experiments suggested predominance of Van der Waals forces for compounds (**1**, **2** and **3**) and Van der Waals forces or hydrogen bond formation for complex (**4**). Thus, complexes (**1-4**) can be stored in the protein and released at targets, in agreement with the behavior reported for other Ru(II)/phosphinic/diiminic complexes.

Evaluation of the antitumor activities showed that the A549 cell line was the most responsive, especially to complex (**3**). Also, complex (**3**) inhibited clonogenic capacity and cell cycle progression of A549 cells and induced apoptosis involving mitochondrial pathway activation. These findings demonstrate that complex (**3**) is a very promising antitumor agent and support further investigations concerning its molecular targets in non-small cell lung cancer.

5. Acknowledgements

The authors thank FINEP, CNPq (448723/2014-0; 308162/2015-3), CAPES, and FAPEMIG (APQ-00273-14; APQ-02486-14; PPM-00533-16) for financial support. We also thank CNPq and CAPES for research fellowships (J.S.M.D.; H.V.R.S.; M.I.F.B.; A.C.D). This work is a collaborative research project by members of the Rede Mineira de Química (RQ-MG), supported by FAPEMIG (RED-00010-14). We also thank Dr. Alzir Azevedo Batista for collaboration in this work.

6. Appendix A. Supplementary data

Coordinates and other crystallographic data have been deposited with CCDC numbers 1831213 and 1831214 for the complex (**5**) and (**6**), respectively. Copies of this information may be obtained from The Director, CCDC, 12 Union Road, Cambridge, CB2 1EZ, UK, Fax: +44 1233 336033, E-mail: deposit@ccdc.cam.ac.uk or www.ccdc.cam.ac.uk.

7. References

[1] G. V. M. Sharma, A. Ramesh, A. Singh, G. Srikanth, V. Jayaram, D. Duscharla, J. H. Jun, R. Ummanni, S. V. Malhotra, Imidazole derivatives show anticancer potential by inducing apoptosis and cellular senescence, Med. Chem. Commun. 5 (2014) 1751-1760.

[2] L. Chen, G. Li, F. Peng, X. Jie, G. Dongye, K. Cai, R. Feng, B. Li, Q. Zeng, K. Lun, J. Chen, B. Xu, The induction of autophagy against mitochondria-mediated apoptosis in lung cancer cells by a ruthenium (II) imidazole complex, Oncotarget. 7 (2016) 80716-80734.

[3] W. M. Motswainyana, P. A. Ajibade, Anticancer Activities of Mononuclear Ruthenium(II) Coordination Complexes, Adv. Chem. 2015 (2015) 1-21.

[4] X. Yang, L. Chen, Y. Liu, Y. Yang, T. Chen, W. Zheng, J. Liu, Q. -Y. He, Ruthenium methylimidazole complexes induced apoptosis in lung cancer A549 cells through intrinsic mitochondrial pathway, Biochimie. 94 (2012) 345-353.

[5]World Health Organization, Cancer-Key Facts. http://www.who.int/mediacentre/factsheets/fs297/en/ , 2018 (accessed 14 February 2018).

[6] F. A. Bhat, Organometallic compounds of ruthenium and their anti-cancer properties, Eur. J. Biomed. Pharm. Sci. 1 (2014) 600-604.

[7] M. P. Chelopo, S. A. Pawar, M. K. Sokhela, T. Govender, H. G. Kruger, G. E. M. Maguire, Anticancer activity of ruthenium(II) arene complexes bearing 1,2,3,4-tetrahydroisoquinoline amino alcohol ligands, Eur. J. Med. Chem. 66 (2013) 407-414.

[8] N. P. E. Barry, P. J. Sadler, Exploration of the medical periodic table: towards new targets, Chem. Commun. 49 (2013) 5106-5131.

[9] V. Brabec, O. Nováková, DNA binding mode of ruthenium complexes and relation ship to tumor cell toxicity, Drug Resistance Updates. 9 (2006) 111-122.

[10] E. S. Antonarakis, A. Emadi, Ruthenium-based chemotherapeutics: are they ready for prime time?, Cancer Chemother. Pharmacol. 66 (2010) 1-9.

[11] A. H. Velders, A. Bergamo, E. Alessio, E. Zangrando, J. G. Haasnoot, C. Casarsa, M. Cocchietto, S. Zorzet, G. Sava, Synthesis and Chemical-Pharmacological Characterization of the Antimetastatic NAMI-A-Type Ru(III) Complexes (Hdmtp)[*trans*-$RuCl_4$(dmso-S)(dmtp)], (Na)[*trans*-$RuCl_4$(dmso-S)(dmtp)], and [*mer*-$RuCl_3(H_2O)$(dmso-S)(dmtp)] (dmtp = 5,7-Dimethyl[1,2,4]triazolo[1,5-*a*]pyrimidine), J. Med. Chem. 47 **(**2004) 1110-1121.

[12] C. G. Hartinger, M. A. Jakupec, S. Z.-Seifried, M. Groessl, A. Egger, W. Berger, H. Zorbas, P. J. Dyson, B. K. Keppler, KP1019, A New Redox-Active Anticancer Agent – Preclinical Development and Results of a Clinical Phase I Study in Tumor Patients, Chemistry & Biodiversity. 5 (2008) 2140-2155.

[13] CrysAlis CCD and CrysAlis Red, Version 171.32.6, Oxford Diffraction Poland, Wrocław, Poland, 2006.

[14] M. C. Burla, R. Caliandro, B. Carrozzini, G. L. Cascarano, C. Cuocci, C. Giacovazzo, M. Mallamo, A. Mazzone, G. Polidori, Crystal structure determination and refinement via SIR2014, J. Appl. Cryst. 48 (2015) 306-309.

[15] G. M. Sheldrick. XS Version 2013/1. Georg-August-Universität Göttingen, Göttingen, 2013.

[16] L. J. Farrugia, WinGX and ORTEP for Windows: an update, J. Appl. Cryst. 45 (2012) 849-854.

[17] C. F. Macrae, I. J. Bruno, J. A. Chisholm, P. R. Edgington, P. McCabe, E. Pidcock, L. R. -Monge, R. Taylor, J. v. Streek, P. A. Wood, Mercury CSD 2.0 – new features for the visualization and investigation of crystal structures, J. Appl. Cryst. 41 (2008) 466-470.

[18] O. V. Dolomanov, L. J. Bourhis, R. J. Gildea, J. A. K. Howard, H. Puschmann, OLEX2: a complete structure solution, refinement and analysis program, J. Appl. Cryst. 42 (2009) 339-341.

[19] S. L. Queiroz, A. A. Batista, G. Oliva, M. T. P. Gambardella, R. H. A. Santos, K. S. MacFarlane, S. J. Rettig, B. R. James, The reactivity of five-coordinate Ru(II) (1,4-bis (diphenylphosphino) butane) complexes with the N-donor ligands: ammonia, pyridine, 4-substituted pyridines, 2,2'-bipyridine, bis(o-pyridyl)amine, 1,10-phenanthroline, 4,7-diphenylphenanthroline and ethylenediamine, Inorg. Chim. Acta. 267 (1998) 209-221.

[20] G. A. Ferreira-Silva, M. M. Ortega, M. A. Banionis, G. Y. Garavelli, F. T. Martins, J. S. M. Dias, C. V. Jr, J. C. Oliveira, F. B. Nascimento, A. C. Doriguetto, M. I. F. Barbosa, M. Ionta, [Ru(pipe)(dppb)(bipy)]PF_6. A novel ruthenium complex that effectively inhibits ERK activation and cyclin D1 expression in A549 cells, Toxicology in Vitro. 44 (2017) 382-391.

[21] N. A. P. Franken, H. M. Rodermond, J. Stap, J. Haveman, C. V. Bree, Clonogenic assay of cells in vitro, Nature Protocols. 1 (2006) 2315-2319.

[22] T. Chen, X. Zhu, Q. Chen, M. Ge, X. Jia, X. Wang, C. Ge, Interaction between Z-ligustilide from Radix Angelica sinensis and human serum albumin, Food Chemistry. 186 (2015) 292-297.

[23] A. P. Carnizello, M. I. F. Barbosa, M. Martins, N. H. Ferreira, P. F. Oliveira, G. M. Magalhães, A. A. Batista, D. C. Tavares, In vitro and in vivo antitumor activity of a novel carbonyl ruthenium compound, the ct-[RuCl(CO)(dppb)(bipy)]PF_6[dppb=1,4-bis(diphenylphosphine)butane and bipy=2,2′-bipyridine], J. Inorg. Biochem. 164 (2016) 42-48.

[24] W. J. Geary, The use of conductivity measurements in organic solventes for the characterisation of coordination compounds, Coord. Chem. Rev. 7 (1971) 81-122.

[25] M. I. F. Barbosa, E. M. A. Valle, S. L. Queiroz, J. Ellena, E. E. Castellano, V. R. S. Malta, J. R. Sousa, O. Piro, M. P. Araujo, A. A. Batista, On the synthesis and structures of the complexes [RuCl(L)(dppb)(N–N)]PF_6 (L = CO, py or 4-NH_2py; dppb = 1,4-bis(diphenylphosphino)butane; N–N = 2,2'-bipyridine or 1,10-phenanthroline) and [(dppb)(CO)Cl_2-Ru-pz-$RuCl_2$(CO)(dppb)] (pz = pyrazine), Polyhedron. 29 (2010) 2297-2303.

[26] C. C. Golfeto, G. V. Poelhsitz, H. S. S. Araújo, M. P. Araujo, J. Ellena, E. E. Castellano, L. G. L. Lopes, I. S. Moreira, A. A. Batista, Synthesis, characterization and cytotoxic activities of the [$RuCl_2$(NO)(dppp)(L)]PF_6 complexes, J. Inorg. Biochem. 104 (2010) 489-495.

[27] T. M. Bastos, M. I. F. Barbosa, M. M. Silva, J. W. C. Júnior, C. S. Meira, E. T. Guimaraes, J. Ellena, D. R. M. Moreira, A. A. Batista, M. B. P. Soares, Nitro/Nitrosyl-ruthenium complexes are potent and selective anti-*Trypanosoma cruzi* agents causing autophagy and necrotic parasite death, antimicrob. Agents Chemother. 58 (2014) 6044-6055.

[28] M. I. F. Barbosa, R. S. Correa, T. M. Bastos, L. V. Pozzi, D. R. M. Moreira, J. Ellena, A. C. Doriguetto, R. G. Silveira, C. R. Oliveira, A. E. Kuznetsov, V. S. Malta, M. B. P. Soares, A. A. Batista, Structural isomerism of Ru(II)-carbonyl complexes: synthesis, characterization and their antitrypanosomal activities, New J. Chem. 41 **(**2017) 4468-4477.

[29] J. P. Barolli, R. S. Corrêa, F. S. Miranda, J. U. Ribeiro, C. B. Jr, J. Ellena, V. Moreno, M. R. Cominetti, A. A. Batista, Polypyridyl Ruthenium Complexes: Novel DNA-Intercalating Agents against Human Breast Tumor, J. Braz. Chem. Soc. 28 (2017) 1879-1889.

[30] J. Lu, A. Holmgren, Thioredoxin system in cell death progression**,** Antioxid. Redox Signaling, 7 (2012) 1738–1747.

[31] F. Basolo, Stabilization of metal complexes by large counter-ions, Coordin. Chem. Rev. 3 (1968) 213-223.

[32] E. R. Santos, M. A. Mondelli, L. V. Pozzi, R. S. Corrêa, H. S. S. Araújo, F. R. Pavan, C. Q. F. Leite, J. Ellena, V. R. S. Malta, S. P. Machado, A. A. Batista, New ruthenium(II)/phosphines/diimines complexes: Promising antitumor (human breast cancer) and Mycobacterium tuberculosis fighting agentes, Polyhedron. 51 (2013) 292-297.

[33] J. B. Godwin, T. J. Meyer, Nitrosyl-Nitrite, Interconversion in Ruthenium Complexes, Inorg. Chem. 10 (1971) 2150-2153.

[34] L. L. Romualdo, A. L. Bogado, E. M. A. Valle, I. S. Moreira, J. Ellena, E. E. Castellano, M. P. Araujo, A. A. Batista, Novel manganese (III) porphyrin containing peripheral ‘‘$[RuCl(dppb)(X\text{-}bipy)]^{+}$’’ cations [dppb = 1,4-bis(diphenylphosphino)butane and X = $–CH_3$, –OMe, –Cl]. X-ray structure of the cis-$[RuCl(dppb)(bipy)(4\text{-}Mepy)]PF_6$ complex, Polyhedron. 27 (2008) 53-58.

[35] F. R. Pavan, G. V. Poelhsitz, M. I. F. Barbosa, S. R. A. Leite, A. A. Batista, J. Ellena, L. S. Sato, S. G. Franzblau, V. Moreno, D. Gambino, C. Q. F. Leite, Ruthenium(II) phosphine/diimine/picolinate complexes: Inorganic compounds as agents against tuberculosis, Eur. J. Med. Chem. 46 (2011) 5099-5107.

[36] L. C. M. Souza, T. A. Santos, C. R. A. Prado, B. A. V. Lima, R. S. Corrêa, A. A. Batista, L. Otubo, J. Ellena, L. T. Ueno, L. R. Dinelli, A. L. Bogado, Influence of gold nanoparticles applied to catalytic hydrogenation of acetophenone with cationic complexes containing ruthenium, *RSC Advances*. 00 (2016) 1-10.

[37] H. V. R. Silva, J. S. M. Dias, G. A. F. Silva, L. C. Vegas, M. Ionta, C. C. Corrêa, A. A. Batista, M. I. F. Barbosa, A. C. Doriguetto, Phosphine/diimine ruthenium complexes with Cl^-, CO, NO^+, NO_2^-, NO_3^- and pyridine ligands: pro-apoptotic activity on triple-negative breast cancer cells and DNA/HSA interactions, Polyhedron. 144 (2018) 55-65.

[38] E. M. A. Valle, B. A. V. Lima, A. G. Ferreira, F. B. Nascimento, V. M. Deflon, I. C. N. Diógenes, U. Abram, J. Ellena, E. E. Castellano, A. A. Batista, Driving forces in substitution reactions of octahedral complexes: The influence of the competitive effect, Polyhedron. 28 (2009) 3473-3478.

[39] V. F. Ferreira, C. R. A. Prado, C. M. Rodrigues, L. Otubo, A. A. Batista, J. W. C. Jr, J. Ellena, L. R. Dinelli, A. L. Bogado, Modified glassy carbon electrode with AuNPs using cis-$[RuCl(dppb)(bipy)(4\text{-}vpy)]^+$ as crossed linking agent, Polyhedron. 78 (2014) 46-53.

[40] I. M. L. Rosa, M. C. S. Costa, B. S. Vitto, L. Amorim, C. C. Correa, C. B. Pinheiro, A. C. Doriguetto, Influence of Synthetic Methods in the Structure and Dimensionality of Coordination Polymers, Cryst. Growth Des. 16 (2016) 1606–1616.

[41] F. H. Herbstein, Crystalline Molecular Complexes and Compounds: Structures and Principles, Oxford University Press, Oxford, 2005.

[42] A. Tarushi, C. P. Raptopoulou, V. Psycharis, A. Terzis, G. Psomas, D. P. Kessissoglou, Zinc(II) complexes of the second-generation quinolone antibacterial drug enrofloxacin: Structure and DNA or albumin interaction, Bioorganic & Medicinal Chemistry. 18 (2010) 2678-2685.

[43] S. –S. Wu, W. –B. Yuan, H. –Y. Wang, Q. Zhang, M. Liu, K. –B. Yu, Synthesis, crystal structure and interaction with DNA and HSA of (N,N'-dibenzylethane-1,2-diamine) transition metal complexes. Inorg. Biochem. 102 (2008) 2026-2034.

[44] J. R. Lakowicz, Topics in Fluorescence Spectroscopy - Biological Applications, Plenum Press, New York, 1992.

[45] L. R. Gouvea, L. S. Garcia, D. R. Lachter, P. R. Nunes, F. C. Pereira, E. P. S. Lacerda, S. R. W. Louro, P. J. S. Barbeira, L. R. Teixeira, Atypical fluoroquinolone gold(III) chelates as potential anticancer agents: Relevance of DNA and protein interactions for their mechanism of action, Eur. J. Med. Chem. 55 (2012) 67-73.

[46] E. Gratton, N. Silva, G. Mei, N. Rosato, I. Savini, A. F. Agro, Fluorescence Lifetime Distribution of Folded and Unfolded Proteins, Int. J. Quantum Chem. 42 (1992) 1479-1489.

[47] Y. Moriyama, D. Ohta, K. Hachiya, Y. Mitsui, K. Takeda, Fluorescence Behavior of Tryptophan Residues of Bovine and Human Serum Albumins in Ionic Surfactant Solutions: A Comparative Study of the Two and One Tryptophan(s) of Bovine and Human Albumins, J. Protein. Chem. 15 (1996) 265-266.

[48] L. C.-Vegas, J. L. Dutra, W. Villarreal, J. H. A. Neto, M. R. Cominetti, F. Pavan, M. Navarro, A. A. Batista, Ru(II)/clotrimazole/diphenylphosphine/bipyridine complexes: Interaction with DNA, BSA and biological potencial against tumor cell lines and Mycobacterium tuberculosis, J. Inorg. Biochem. 162 (2016) 135-145.

[49] S. W. Chang, A. R. Lewis, K. E. Prosser, J. R. Thompson, M. Gladkikh, M. B. Bally, J. J. Warren, C. J. Walsby, CF3 Derivatives of the Anticancer Ru(III) Complexes KP1019, NKP-1339, and Their Imidazole and Pyridine Analogues Show Enhanced Lipophilicity, Albumin Interactions, and Cytotoxicity, Inorg. Chem. 55 (2016) 4850-4863.

[50] D. Sun, Z. Mou, N. Li, W. Zhang, Y. Wang, E. Yang, W. Wang, Anti-tumor activity and mechanism of apoptosis of A549 induced by ruthenium complex, J. Biol. Inorg. Chem. 21 (2016) 945-956.

[51] M. Reck, D. F. Heigener, T. Mok, J. C. Soria, K. F. Rabe, Management of non-small-cell lung cancer: recent developments, The Lancet. 382 (2013) 709-719.

[52] C. S. Leung, S. S. F. Leung, J. T.-Rives, W. L. Jorgensen, Methyl Effects on Protein−Ligand Binding, J. Med. Chem. 55 (2012) 4489-4500.

[53] D. Hanahan, R. A. Weinberg, Hallmarks of Cancer: The Next Generation, Cell. 144 (2011) 646-674.

[54] A. P. Lima, F. C. Pereira, C. A. S. T. V. Costa, J. R. Soares, L. C. G. Pereira, H. K. P. Porto, L. A. Pavanin, W. B. Santos, E. P. S. Lacerda, Induction of Cell Cycle Arrest and Apoptosis by Ruthenium Complex cis-(Dichloro)tetramineruthenium(III) Chloride in Human Lung Carcinoma Cells A549, Biol. Trace Elem. Res. 147 (2012) 8-15.

[55] E. K. Cassimere, C. Mauvais, C. Denicourt, $p27^{Kip1}$ Is Required to Mediate a G1 Cell Cycle Arrest Downstream of ATM following Genotoxic Stress, PLOS ONE. 11 (2016) 1-20.

[56] J. Chen, Y. Zhang, G. Li, F. Peng, X. Jie, J. She, G. Dongye, Z. Zou, S. Rong, L. Chen, Cytotoxicity in vitro, cellular uptake, localization and apoptotic mechanism studies induced by ruthenium(II) complex, J. Biol. Inorg. Chem. 23 (2017) 261-275.

[57] C. O. D. S. Costa, J. H. A. Neto, I. R. S. Baliza, R. B. Dias, L. F. Valverde, M. T. A. Vidal, C. B. S. Sales, C. A. G. Rocha, D. R. M. Moreira, M. B. P. Soares, A. A. Batista, D. P. Bezerra, Novel piplartine-containing ruthenium complexes: synthesis, cell growth inhibition, apoptosis induction and ROS production on HCT116 cells Oncotarget. 8 (2017) 104367-104392.

[58] D. Vecchio, G. Frosina, Targeting the Ataxia Telangiectasia Mutated Protein in Cancer Therapy, Curr. Drug. Targets. 17 (2016) 139-153.

Figure legend

Scheme 1: Synthetic route of complexes (**1-4**).

Figure 1: Plots with partial atom labeling showing the cationic part of the asymmetric unit of (**5**) **(a)** and (**6**) **(b)** and the superposition of the compound backbones created by selecting the Ru atoms and the six atoms coordinated to them as homologous atom pairs **(c)**. The H atoms, hexafluorophosphate anion and solvating methanol (present in (**6**)) were omitted for the sake of clarity. Ellipsoid plots with complete atom labeling for (**5**) and **(6)** are given in (Supporting material: **Figure 34S**).

Figure 2: A molecular superposition of (**6**) (in orange) and its *cis*-[RuCl(4-vinylpyridine)(dppb)(5,5`-Mebipy)] analogue (CCDC code BUZYIF [38] in light green) created by selecting the Ru atoms and the six atoms coordinated to them as homologous atom pairs. Hydrogen atoms are omitted for clarity.

Figure 3: Partial packing of (**6**) **(a)** and its *cis*-[RuCl(4-vinylpyridine)(dppb)(5,5`-Mebipy)] analogue (CCDC code BUZYIF [38]) **(b)** projected onto their respective *ab* planes highlighting the equivalence of their intermolecular arrays. The cationic complex and the hexafluorophosphate anion are depicted in green and blue, respectively. The black dotted circles highlight the region occupied by the 1Meim + methanol (in red) in (**6**) or by the 4-vinylpyridine in the analogous structure depicted in (**b**). Hydrogen atoms (excepted to those bind to methanol) were omitted for the sake of clarity.

Figure 4: Changes in the electronic absorption spectra of (**3**) with increasing concentrations of ctDNA. [3] = 1.00×10^{-3} M and [ctDNA] = 0 – 3.78×10^{-5} M in Tris-HCl buffer (5 mM Tris–HCl and 50 mM NaCl, pH 7.4) at 298 K.

Figure 5: **(A)** A549 cell viability determined by MTS assay after 24h of treatment with different compounds at 20 µM or 40 µM. **(B)** Concentration-response curves of the complex (**3**), their precursor, and free 1-methylimidazole. *p < 0.05, **p < 0.01 and ***p < 0.001 determined using ANOVA followed by Tukey's post-test from three independent experiments.

Figure 6: **(A)** Illustrative image showing the morphological features of A549 cultures obtained by phase contrast microscopy (60× magnification). **(B)** Illustrative images and quantitative data from the clonogenic assay. **(C)** Representative histograms obtained by flow cytometry showing cell populations in different cell cycle phases. Brown (Sub-G1 phase), pink (G0/G1 phases), green (S phase), blue (G2/M phase). **(D)** Dot plots from the annexin V/7-AAD assays. Viable cells (lower left quadrants), early apoptosis (lower right quadrants), late apoptosis (upper right quadrants), and nonviable cells (necrotic cells) (upper left quadrants). (E) Mitochondrial membrane potential assay using JC-1 as a fluorescent probe. CCCP was used as a positive control to reduce $\Delta\Psi m$. (F) ATM activation was determined by measuring ATM phosphorylation levels at Ser1981. *p < 0.05, and ***p < 0.001 determined using ANOVA followed by Tukey's post-test from three independent experiments.

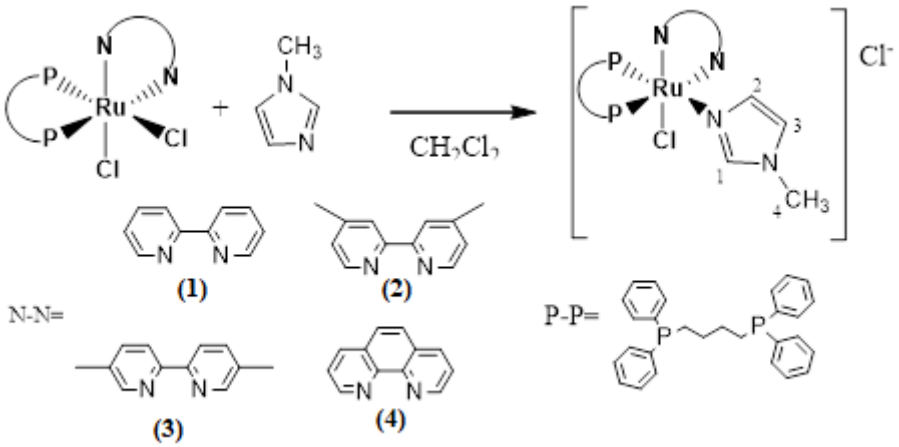

Scheme 1.

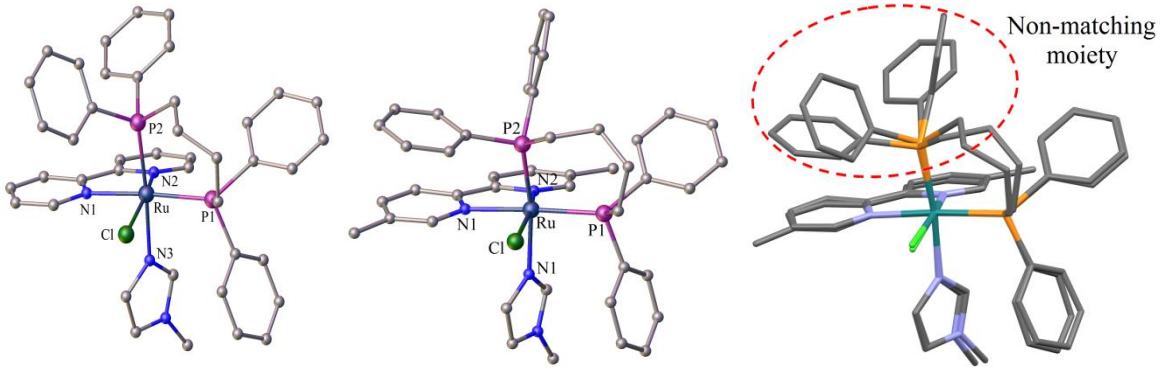

(a) **(b)** **(c)**

Figure 1.

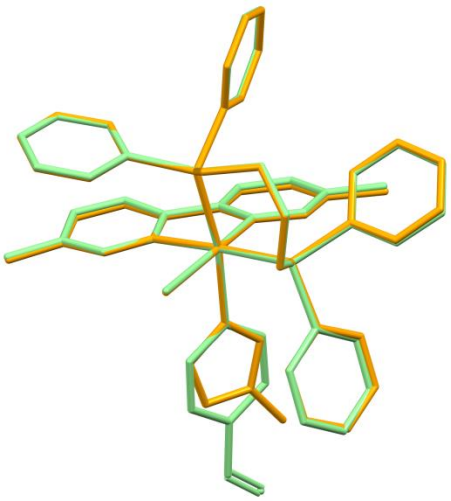

Figure 2.

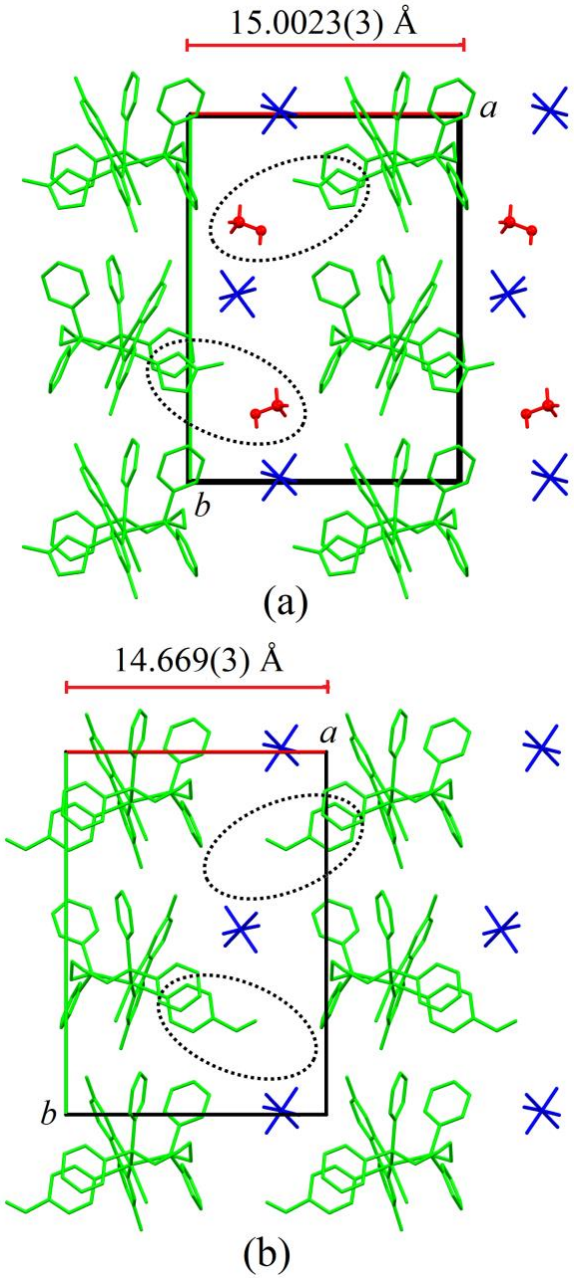

Figure 3.

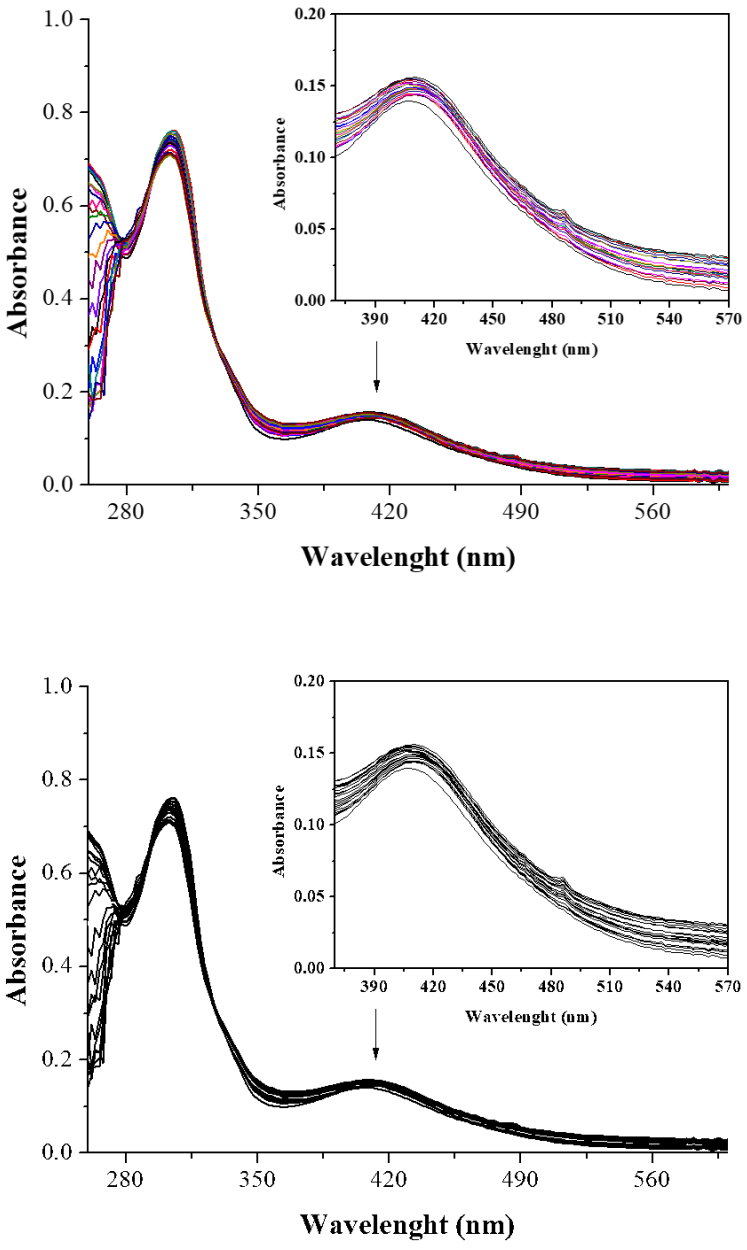

Figure 4.

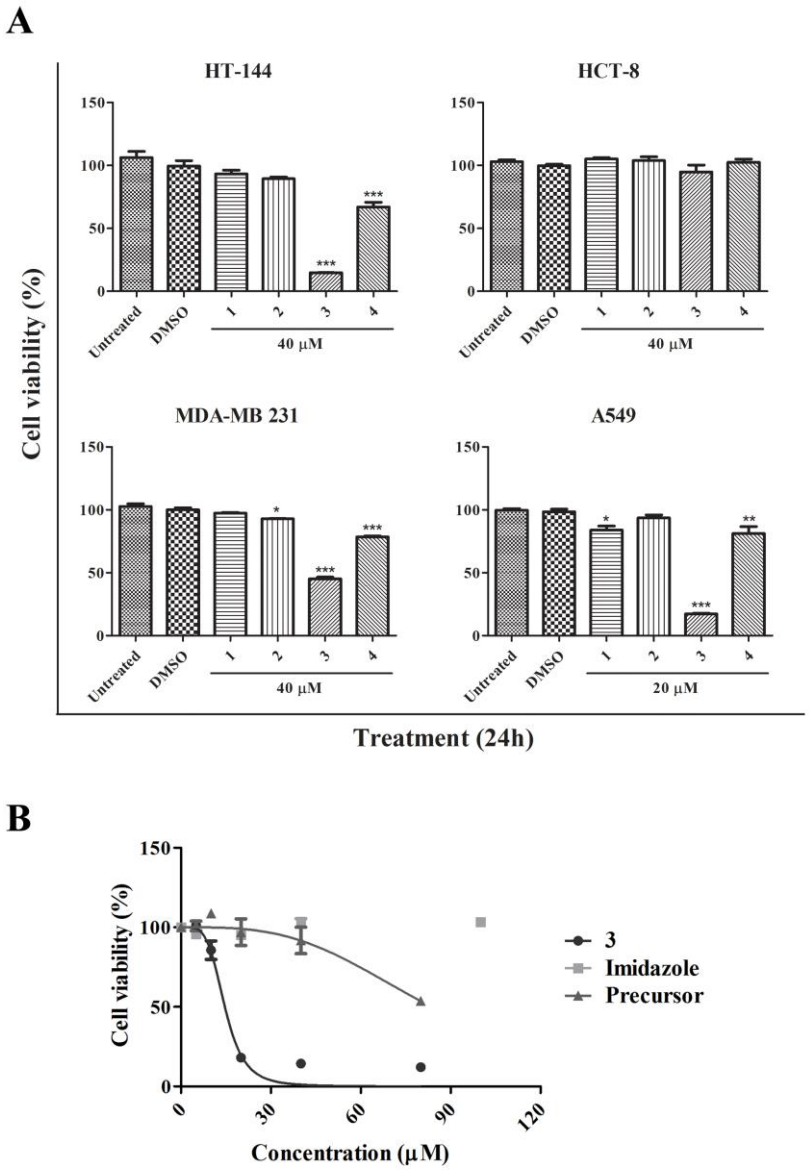

Figure 5.

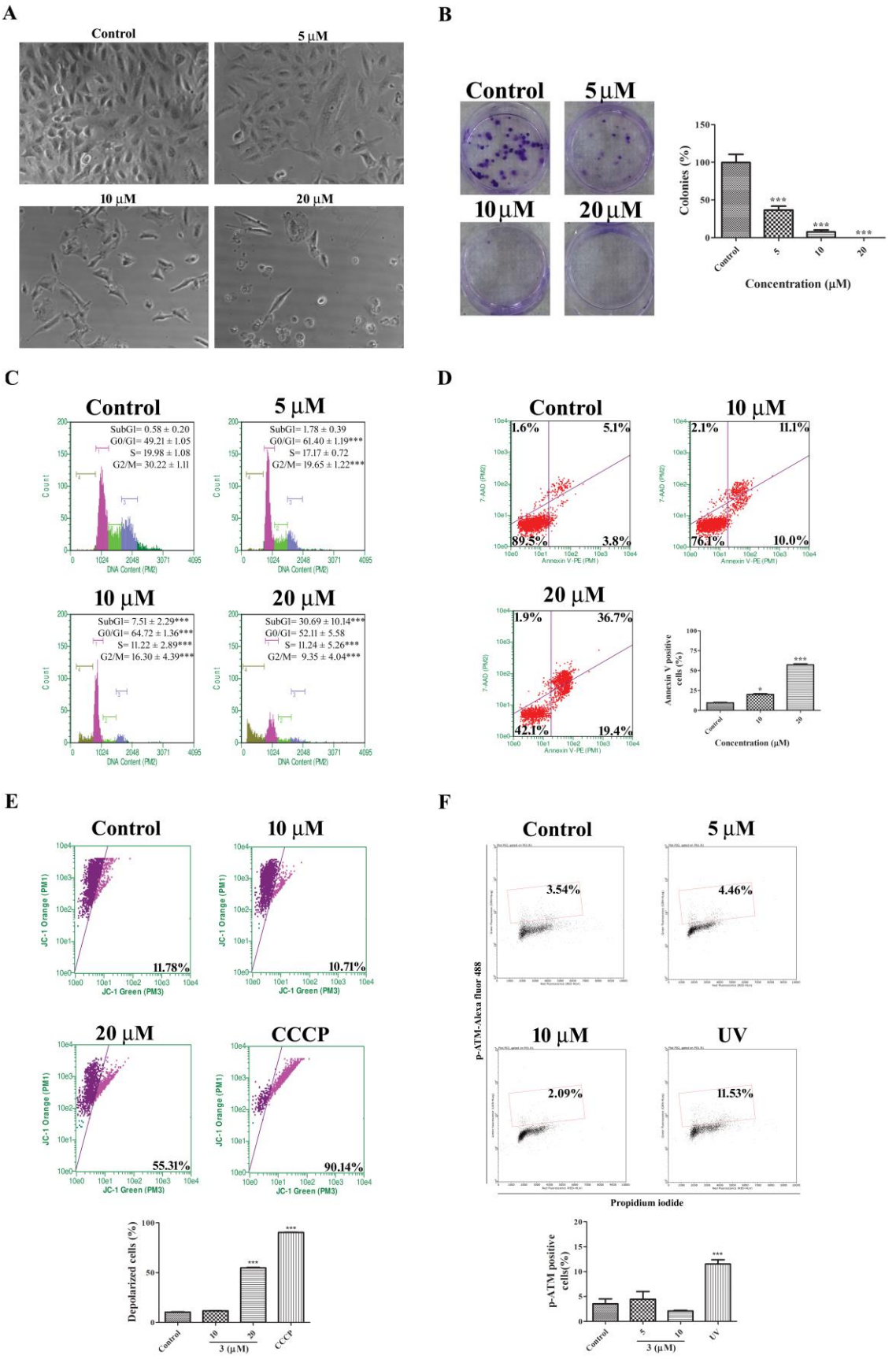

Figure 6.

Table 1. Crystal data and structure refinement for (**5**) and (**6**).

	(**5**)	(**6**)
Empirical formula	$(C_{42}H_{42}Cl_1N_4O_1P_2Ru_1)^+$ $(P_1F_6)^-$	$(C_{44}H_{46}Cl_1N_4P_2Ru_1)^+$ $(P_1F_6)^-.(C_1H_4O_1)$
Formula weight	946.22	1006.32
Temperature (K)	298(2)	298(2)
Wavelength (Å)	0.71073	0.71073
Crystal system	Orthorhombic	Orthorhombic
Space group	$Pca2_1$	Pbca
Unit cell dimensions (Å)	*a* = 17.0144(3) *b* = 15.0566(3) *c* = 16.6356(3)	*a* = 15.0023(3) *b* = 20.3898(3) *c* = 29.2586(6)
Volume ($Å^3$)	4261.69(14)	8950.0(3)
Z	4	8
Calc. Density (Mg/m^3)	1.475	1.494
Absorption coef. (mm^{-1})	0.605	00.582
F(000)	1928	4128
θ range for data collection (°)	3.426 to 29.771	3.256 to 29.787
Index ranges	-23<=h<=23, -20<=k<=21, -22<=l<=21	20<=h<=20, -25<=k<=28, -40<=l<=40
Reflections collected	99970	191069
Independent reflections	11162 [R(int) = 0.0553]	12270 [R(int) = 0.0532]
Completeness to θ max. (%)	99.7	99.8
Data/restraints/parameters	11162 / 1 / 514	12270 / 0 / 552
Goodness-of-fit on F^2	1.026	1.129
Final R indices [I>2σ(I)]	R1 = 0.0409, wR2 = 0.0863	R1 = 0.0583, wR2 = 0.1250
R indices (all data)	R1 = 0.0587, wR2 = 0.0944	R1 = 0.0832, wR2 = 0.1376
Largest diff. peak and hole ($e.Å^{-3}$)	0.524 and -0.315	0.780 and -0.642

Table 2. Main IR frequencies (cm^{-1}) of 1-methylimidazole and complexes (**1**-**4**).

Assignation	**1Meim**	**1**	**2**	**3**	**4**
ν (C-H) (w)	3112	3126	3128	3132	3126
ν (C=N) (bs)	1649	1629	1622	1624	1625
ν (C=C) (s)	1521	1535	1533	1535	1535
ν (C-N)$_{arom}$ (s)	1286	1280	1282	1284	1282
ν (C-N)$_{alif}$ (s)	1232	1230	1236	1232	1230
δ (C-H) (s)	827-748	816-741	827-741	816-740	814-741
ν(Ru-P) (m)	-	520-507	519-507	518-507	520-507
ν(Ru-N) (w)	-	489	485	489	487
ν(Ru-Cl) (w)	-	295	-	-	-

Abbreviations: s, strong; m, medium; w, weak; b, broad.

Table 3. Selected bond lengths and angles for (**5**) and (**6**).

Bond (Å)		
	(**5**)	(**6**)
Ru-N1	2.112(4)	2.125(3)
Ru-N2	2.074(4)	2.069(3)
Ru-N3	2.176(4)	2.170(3)
Ru-P1	2.355(1)	2.338(1)
Ru-P2	2.323(1)	2.315(1)
Ru-Cl	2.419(1)	2.4347(9)
Angles (°)		
	(**5**)	(**6**)
N3-Ru-N1	84.9(2)	83.0(1)
N3-Ru-N2	82.5(1)	84.0(1)
N3-Ru-P1	92.5(1)	93.94(8)
N3-Ru-P2	175.5(1)	170.14(8)
N3-Ru-Cl	85.2(1)	87.39(8)
Cl-Ru-N1	91.2(1)	92.19(7)
Cl-Ru-N2	164.2(1)	167.68(8)
Cl-Ru-P1	86.11(4)	88.22(3)
Cl-Ru-P2	95.37(4)	86.05(3)
P1-Ru-N1	176.4(1)	176.91(8)
P1-Ru-N2	104.2(1)	101.15(8)
P1-Ru-P2	92.06(4)	93.20(3)
P2-Ru-N1	90.6(1)	89.88(8)
P2-Ru-N2	96.2(1)	101.23(8)
N1-Ru-N2	77.9(2)	78.0(1)

Table 4. Stern–Volmer quenching constant ($K_{sv,}$ M^{-1}), biomolecular quenching rate constant (Kq, M^{-1} s^{-1}), binding constant (Kb, M^{-1}), number of binding sites (n), ΔG° (KJ·mol^{-1}), ΔH° (KJ·mol^{-1}) and ΔS° (J·mol^{-1}·K) for the complex–HSA systems at different temperatures.

Complexes	Tem. (K)	Ksv (10^4mol·L^{-1})	Kb (mol·L^{-1})	n	ΔG°	ΔH°	ΔS°
1	**298**	2.31 ± 0.002	$5.16 \cdot 10^4$ ± 1.99	1.09 ± 0.08	-26.89	-69.26	-142.18
	310	1.73 ± 0.09	$1.75 \cdot 10^4$ ± 1.68	1.00 ± 0.05	-25.18		
2	**298**	4.39 ± 0.08	$1.97 \cdot 10^5$ ± 1.72	1.16 ± 0.05	-30.21	-7.12	-77.47
	310	3.41 ± 0.03	$1.77 \cdot 10^5$ ± 2.13	1.17 ± 0.07	-31.14		
3	**298**	9.15 ± 0.001	$1.77 \cdot 10^6$ ± 1.50	1.32 ± 0.04	-35.65	-99.50	-214.27
	310	5.78 ± 0.07	$3.75 \cdot 10^5$ ± 1.36	1.19 ± 0.03	-33.08		
4	**298**	21.50 ± 0.003	$1.71 \cdot 10^8$ ± 1.20	1.70 ± 0.02	-46.96	185.48	780.00
	310	17.00 ± 0.09	$3.09 \cdot 10^9$ ± 1.14	1.98 ± 0.01	-56.32		

Table 5. Binding constants (K_b) and hypochromism percentage (%H) of compounds (**1-4**).

Compounds	K_b (10^5 M^{-1})	% H
1	3.10 ± 0.37	7.23
2	3.21 ± 0,05	4.32
3	1.83 ± 0.04	12.02
4	0.20 ± 0.06	3.03

Table 6. IC_{50} values (μM) determined from MTS data after 24 h of treatment.

Compounds	A549	CCD-1059Sk	SI**
1Meim	n.d.	n.d	-
Complex (3)	14.65 ± 0.90	35.68 ± 0.79	2.39
Precursor	n.d.	n.d	-
Cisplatin*	59.54 ± 5.45	74.25 ± 5.26	1.25

* Cisplatin was used as a positive control; n.d: not determined because the reduction in cell viability was not enough for determining IC_{50} values. ** Selectivity index represents the ratio between the IC_{50} values obtained for the normal cell line and the tumor cell line.

Graphical abstract

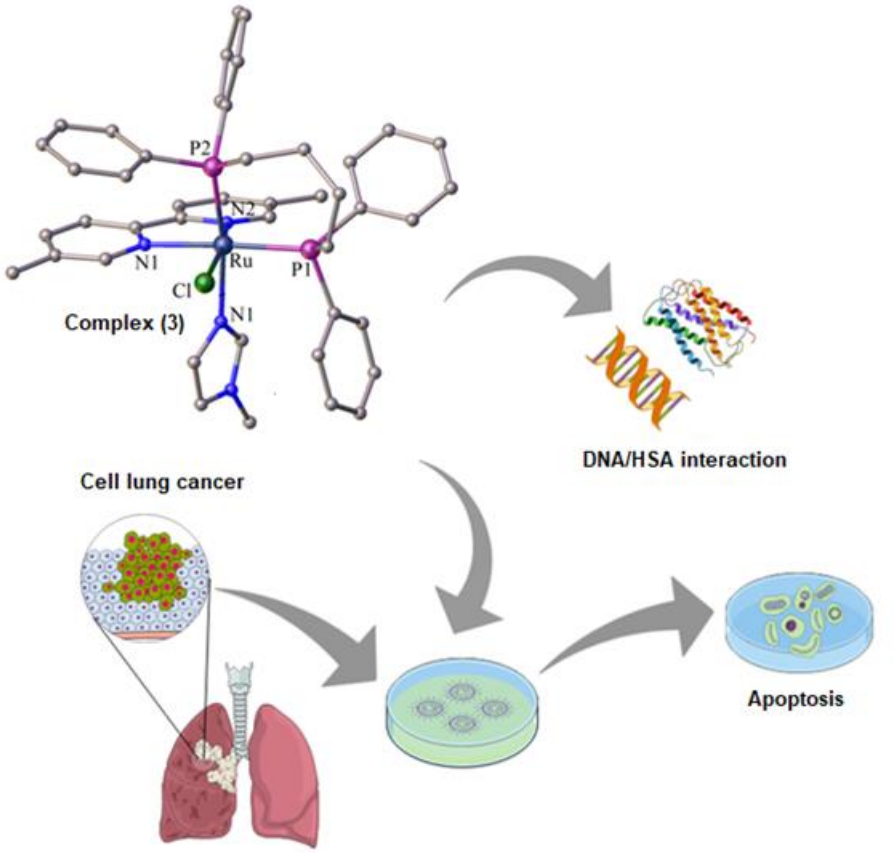

Ruthenium(II) complexes with 1-methylimidazole as ligand were obtained. DNA and human serum albumin interactions were evaluated. The complex **(3)** presented higher cytotoxic activity that was correlated with pro-apoptotic potential.

Highlights

- Novel ruthenium(II) complexes containing 1-methylimidazole as ligand were obtained.
- Interactions with DNA and human serum albumin (HSA) were performed.
- Cytotoxicity profiles were determined for different tumor cell lines.
- Complex (**3**) presented higher cytotoxic activity in non-small cell lung cancer.